

CodEx: A Modular Framework for Joint Temporal De-blurring and Tomographic Reconstruction

Soumendu Majee, *Student Member, IEEE*, Selin Aslan, Charles A. Bouman *Fellow, IEEE*,
Doğa Gürsoy *Member, IEEE*

Abstract—In many computed tomography (CT) imaging applications, it is important to rapidly collect data from an object that is moving or changing with time. Tomographic acquisition is generally assumed to be step-and-shoot, where the object is rotated to each desired angle, and a view is taken. However, step-and-shoot acquisition is slow and can waste photons, so in practice fly-scanning is done where the object is continuously rotated while collecting data. However, this can result in motion-blurred views and consequently reconstructions with severe motion artifacts.

In this paper, we introduce CodEx, a modular framework for joint de-blurring and tomographic reconstruction that can effectively invert the motion blur introduced in fly-scanning. The method is a synergistic combination of a novel acquisition method with a novel non-convex Bayesian reconstruction algorithm. CodEx works by encoding the acquisition with a known binary code that the reconstruction algorithm then inverts. Using a well chosen binary code to encode the measurements can improve the accuracy of the inversion process. The CodEx reconstruction method uses the alternating direction method of multipliers (ADMM) to split the inverse problem into iterative deblurring and reconstruction sub-problems, making reconstruction practical to implement. We present reconstruction results on both simulated and experimental data to demonstrate the effectiveness of our method.

Index Terms—Computed tomography, Coded exposure, Inverse Problems, MBIR, Motion-invariant imaging, Deblurring, ADMM

I. INTRODUCTION

Computed tomography (CT) imaging has been widely used in a variety of applications to study the internal structure of static and dynamic objects. For rapidly changing objects, good temporal resolution is crucial in order to resolve the reconstructed object accurately. Model based iterative reconstruction (MBIR) [1] techniques have led to significant improvements in temporal resolution for time-resolved CT through the use of novel view-sampling [2] and improved prior modeling [2]–[4]. However, even with these improvements, the temporal

resolution is fundamentally limited by the rate of collection of projection measurements.

In an ideal CT system, each view is assumed to measure the projection at a single angle. A step-and-shoot acquisition strategy conforms with this assumption by rotating the object to each desired angle and stopping the rotation before taking a measurement. However, a disadvantage of step-and-shoot is that photons can not be collected during rotation and the exposure time must be short relative to the motion of the stage. Consequently, if the mechanical settling time of the rotating stage is long, then step-and-shoot acquisition will be slow and photon flux will be wasted.

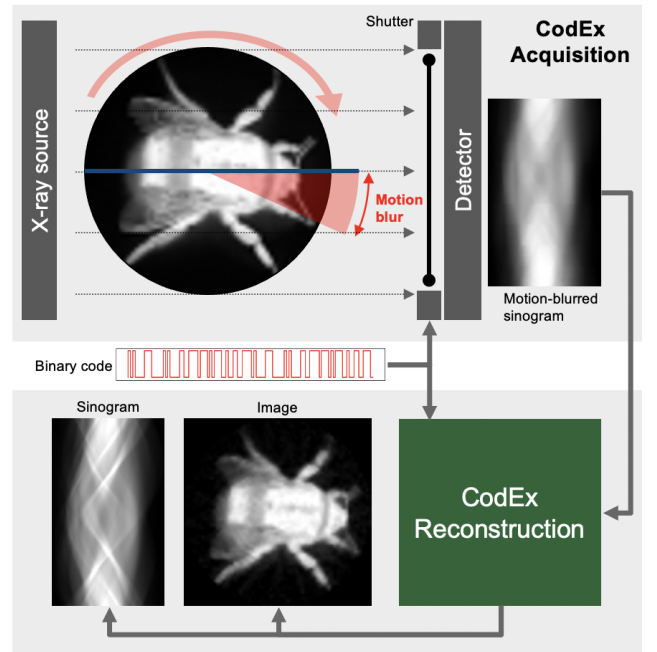


Figure 1. Illustration of our method, CodEx. CodEx is a synergistic combination of a coded acquisition and a non-convex Bayesian reconstruction. During acquisition, CodEx flutters the exposure on and off rapidly in a known binary code during each view, resulting in a coded motion blur. CodEx reconstruction uses the knowledge of the code to effectively invert the coded motion blur. A well chosen code can improve the accuracy of CodEx reconstruction, but CodEx can improve the reconstruction quality even without coding by inverting the motion blur due to fly-scanning.

A more practical acquisition strategy is fly-scanning [5] where the object rotates continuously and exposures are taken with 100% duty cycle so that no photon flux is wasted.

Soumendu Majee is with the Applied Mathematics and Plasma Physics Group at Los Alamos National Laboratory (e-mail: smajee@lanl.gov). Selin Aslan is with the X-ray Science Division, Argonne National Laboratory (e-mail: selinaslanphd@gmail.com). Charles A. Bouman is with the School of Electrical and Computer Engineering, Purdue University (e-mail: bouman@purdue.edu). Doga Gürsoy is with the X-ray Science Division, Argonne National Laboratory and the Electrical Engineering and Computer Science Department, Northwestern University (e-mail: dgursoy@anl.gov).

This research used resources of the Advanced Photon Source, a U.S. Department of Energy (DOE) Office of Science User Facility operated for the DOE Office of Science by Argonne National Laboratory under Contract No. DE-AC02-06CH11357. This work was partially supported by an NSF grant number CCF-1763896.

However, a disadvantage of fly-scanning is that views have motion blur, and the associated reconstructions contain blur and motion artifacts.

Pre-processing based approaches have been proposed in the literature to mitigate the motion blur in the measurements caused by fly-scanning. Chang et al. [6] proposed a linear pre-processing of the measurements as well as post-processing of the reconstruction in order to reduce the motion artifacts due to fly-scanning. However, the linear processing introduces additional artifacts in some cases. Chen et al. [7] proposed an optimization based deblurring in the radiograph domain followed by reconstruction using a conventional analytical reconstruction method. The deblurring is done by solving a map estimation problem in the radiograph domain using a linear blurring based forward model and a total variation (TV) prior on the radiographs. The authors demonstrated that their method can substantially reduce blurring artifacts due to fly-scanning in reconstructions. However, the method requires that dense view samples be taken that are finely spaced in angle using multiple rotations of the object. The method is not as appropriate when the views are sparsely sampled since the deblurring problem becomes ill-posed in this case.

Another set of approaches for reducing fly-scanning artifacts is to model the motion blur within a model based reconstruction framework and reconstruct the underlying image by inverting the blur model. Cant et al. [8] approximate the non-linear blur due to fly-scanning as a linear operation in the projection domain. The combined linear measurement model is then inverted via simultaneous iterative reconstruction algorithm (SIRT) [9]. Alternatively, Tilley et al. [10] use a non-linear forward model in a model-based reconstruction framework, and then perform tomographic inversion by minimizing the resulting non-convex cost function. In order to improve the accuracy of the inversion process, Ching et al. [11] propose to modulate each view by a binary code. The authors approximate the resulting coded non-linear blur as a linear operation and perform reconstruction using a modified version of the algebraic reconstruction technique (ART) [12]. While these approaches have been demonstrated to help remove the effects of motion blur, they are primarily designed for the case when view sampling is dense.

In this paper, we introduce CodEx, a modular framework for joint de-blurring and non-linear tomographic reconstruction that can effectively invert the motion blur introduced in fly-scanning. Figure 1 illustrates our approach. During acquisition, CodEx flutters the exposure on and off in a known binary code during each view. This results in a coded motion blur that is easily inverted [13].

CodEx subsequently uses the knowledge of the code to solve a non-convex iterative reconstruction problem using the alternating direction method of multipliers (ADMM) algorithm. The resulting CodEx algorithm iteratively applies a non-linear deblurring operation followed by a model based iterative reconstruction (MBIR) [1] operation. This results in a modular reconstruction algorithm that can be easily adapted to different CT geometries.

The novel contributions of this paper are:

- 1) A modular reconstruction approach using ADMM for

the nonlinear reconstruction of sparse-view transmission CT data;

- 2) A coded exposure measurement scheme for collection of sparse transmission CT data;
- 3) An interlaced view-sampling approach for progressively collecting sparse CT view data.

We present results on simulated as well as experimental data that demonstrate that the CodEx method can dramatically improve reconstruction quality as compared to conventional reconstruction. We also show that the method has the greatest benefit at low photon counts.

The rest of the paper is organized as follows. In section II, we introduce the general problem of motion blur due to integration over angles, as well as coded acquisition in order to mitigate the effect of the motion blur. In section III, we introduce our CodEx formulation that models the coded motion blur and inverts it during the reconstruction process. In section IV, we describe our interlaced view-angle sampling scheme that provides a practical approach for performing coded exposure acquisition with interlaced view angles. Finally, in section V, we present results on simulated and experimental data to evaluate our method.

II. CT FLY SCANNING

In a conventional computed tomography (CT) setting, a single view is assumed to measure the projection of an object at a single angle. To conform with this assumption, a step-and-shoot scanning is done where the object is rotated to each desired angle, a view measurement is taken, and the rotation is resumed. However, this leads to slow acquisition and wasted photons. A more practical approach is fly-scanning, where the object is continuously rotated while the view measurements are being taken. However, in this case, the detector integrates the incoming photon-flux over a range of angles instead of a single angle, as shown in Figure 2. The resulting vector of M_d expected photon-counts at the detector at angle θ_0 can be written as

$$\bar{\lambda}_{\theta_0}^{\text{boxcar}} = \frac{\lambda^0}{\Delta\theta} \int_{\theta_0}^{\theta_0+\Delta\theta} \exp\{-A_\theta x\} d\theta, \quad (1)$$

where $A_\theta \in \mathbb{R}^{M_d \times N}$ performs the forward projection of the image x at angle θ , λ^0 is the photon-flux of the X-ray source, and $\Delta\theta$ is the blur-angle. The super-script boxcar refers to the standard exposure where the detector shutter is on throughout the acquisition.

We can approximate the integration in equation (1) using a discrete sum over K closely spaced angles as

$$\bar{\lambda}_{\theta_0}^{\text{boxcar}} = \frac{\lambda^0}{K} \sum_{k=0}^{K-1} \exp\left\{-A_{\theta_0 + \frac{k\Delta\theta}{K}} x\right\}. \quad (2)$$

We will refer to these K closely spaced angles as micro-projection angles henceforth.

As $\Delta\theta$ becomes larger, we collect more photons in a single measurement, but this comes at the cost of blurred measurements, which leads to a reconstruction with motion artifacts. To overcome this problem, our approach will be to modulate the photon flux at each of the K micro-projection

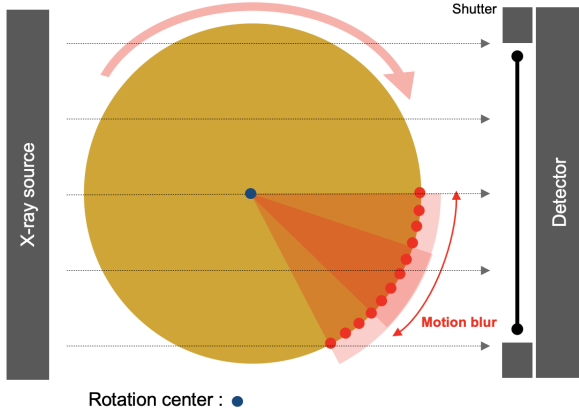


Figure 2. Illustration of motion blur due to rotation. In fly-scanning, the detector integrates photons over a range of projection angles (red sector). This integration can be approximated as a discrete sum over closely spaced micro-projection angles (red dots).

angles by a binary code. This can be done by pulsating the X-ray source [14], using the electronic shutter of the detector sensor, or with a mechanical shutter on the beam path [15] as shown in Figure 2. In this case, the expected photon-counts at the detector at angle θ_0 can be written as

$$\bar{\lambda}_{\theta_0} = \frac{\lambda^0}{K} \sum_{k=0}^{K-1} c_k \exp \left\{ -A_{\theta_0 + \frac{k\Delta\theta}{K}} x \right\}, \quad (3)$$

where $c = [c_0, c_1, \dots, c_{K-1}]$ is the binary code used to modulate the photons. In this case, each measurement is formed by a coded sum over K non-overlapping micro-projection angles. Notice that equation (3) reduces to the boxcar case of equation (2) when $c = [1, 1, \dots, 1]$. On the other hand, equation (3) reduces to step-and-shoot scanning when $c = [1, 0, \dots, 0]$. Modulating the photon flux results in loss of photons compared to the boxcar case of $c = [1, 1, \dots, 1]$, but many more photons are collected relative to the step-and-shoot case of $c = [1, 0, \dots, 0]$. A good choice of code c can result in an invertible blur while improving the signal to noise ratio (SNR) of the measurements.

III. CODEX FORMULATION

In this section, we will introduce CodEx, a synergistic combination of coded acquisition and CT reconstruction. During the acquisition process, we collect M_θ 2D radiograph measurements at M_θ different measurement angles. As Figure 2 illustrates, each radiograph measures the projection of the object across a range of angles which can be written as a function of K micro-projections. Some of the M_θ measurements can have overlapping projections and share the same micro-projections. Without loss of generality, we assume that there are $N_\theta \leq KM_\theta$ unique micro-projection angles in $[0, \pi]$ out of the KM_θ maximum possible micro-projection angles.

A. Data Likelihood Model

For each measurement, we use a binary code $c = [c_0, c_1, \dots, c_{K-1}]$ to modulate the photon-flux over K micro-projection angles as shown in equation (3). The resulting

vector of expected photon counts for all the measurement angles can be written as

$$\bar{\lambda} = \bar{c} \frac{\lambda^0}{K} C \exp \{-Ax\}, \quad (4)$$

where, $\bar{\lambda} \in \mathbb{R}^{M_\theta M_d}$ is the vector of expected photon counts for the M_θ measurement angles and M_d detector pixels, $C \in \mathbb{R}^{M_\theta M_d \times N_\theta M_d}$ is a sparse matrix that performs the coded sum in equation (3) and is normalized such that each row of C sums to 1, $\bar{c} = \sum_{k=0}^{K-1} c_k$ is the normalizing constant, $A \in \mathbb{R}^{N_\theta M_d \times N}$ projects the image $x \in \mathbb{R}^N$ for the N_θ unique micro-projection angles. The structure of the matrix C depends on how the M_θ measurement angles are arranged, and how each measurement relates to the micro-projections at K micro-projection angles. Section IV provides details on the structure of C for a practical interlaced view-sampling strategy.

The vector of incident photon counts at the detector, $\lambda \in \mathbb{R}^{M_d M_\theta}$ are given by

$$\lambda \sim \text{Pois}(\bar{\lambda}), \quad (5)$$

where $\text{Pois}(\bar{\lambda})$ denotes an element wise Poisson distribution with mean $\bar{\lambda}$. A high expected photon-count $\bar{\lambda}$ results in a higher signal to noise ratio (SNR) in the measurements. The goal of the coded projections is to increase the SNR of the acquired data while also allowing for accurate deblurring of the summed micro-projections. A good code c introduces an invertible blur and allows us to preserve high frequency information while at the same time collecting more photons to reduce noise [13].

In order to derive the forward model, we first convert the photon-count measurements into projection measurements as is typically done in tomography. In order to do this, we normalize by the ‘‘blank scan’’ obtained when the object is removed (i.e., $x = 0$), and we take the negative log to form

$$y = -\log \left\{ \frac{\lambda}{\bar{c} \lambda^0 / K} \right\}, \quad (6)$$

where $y \in \mathbb{R}^{M_d M_\theta}$ is the vector of projection measurements for all M_θ views, and $\bar{c} = \sum_{i=0}^{K-1} c_k$ results from the assumption that $x = 0$ in equation (3). If the photon counts are large, then we can make the approximation [1], [16] that

$$\begin{aligned} E[y|x] &\approx -\log \{C \exp \{-Ax\}\} \\ \text{Var}[y|x] &\approx D^{-1}. \end{aligned} \quad (7)$$

where $D = \text{diag}\{\lambda\}$. In practice, the true photon counts, λ are often unknown. Consequently, we set the precision matrix D as

$$D = \text{diag}\{w \exp \{-y\}\}, \quad (8)$$

where the scalar w is empirically chosen [2], [16].

Using a second order Taylor series approximation [1] to the Poisson log-likelihood function, we can write the log-likelihood function as

$$-\log p(y|x) = \frac{1}{2} \|y + \log \{C \exp \{-Ax\}\}\|_D^2 + \text{const}(y). \quad (9)$$

Here $\text{const}(y)$ refers to constant terms that are not a function of x and can thus be ignored while optimizing with respect to x .

B. MAP Estimate

The X-ray attenuation coefficient image x^* can be reconstructed by computing a Maximum A Posteriori (MAP) estimate as

$$\begin{aligned} x^* &= \arg \min_x \{-\log p(y|x) - \log p(x)\} \\ &= \arg \min_x \left\{ \frac{1}{2} \|y + \log \{C \exp \{-Ax\}\}\|_D^2 + h(x) \right\} \end{aligned} \quad (10)$$

where $h(x)$ is the regularization or prior model [4], [17] and the data likelihood term $-\log p(y|x)$ follows from equation (9). Notice that the non-linear logarithmic and exponential terms make direct optimization of the cost function in equation (10) challenging. However, in the following sections, we propose a modular algorithm for solving (10) that makes the solution practical to implement.

C. ADMM Formulation

In order to simplify the optimization in equation (10), we split the cost function into two parts with the following constraint

$$p = Ax, \quad (11)$$

where $p \in \mathbb{R}^{N_\theta M_d}$ is the projection of the image x at the N_θ finely spaced micro-projection angles. In other words, p is the full set of unobserved micro-projections of the object. We thus form the following equivalent problem.

$$\begin{aligned} x^*, p^* &= \arg \min_{x,p} \left\{ \frac{1}{2} \|y + \log \{C \exp \{-p\}\}\|_D^2 + h(x) \right\} \\ \text{s.t } p &= Ax \end{aligned} \quad (12)$$

Next, we will use the alternating directions method of multipliers (ADMM) method [18] to solve the constrained optimization of equation (12). The augmented Lagrangian for this problem is given by

$$\begin{aligned} L(p, x, u) &= \frac{1}{2} \|y + \log \{C \exp \{-p\}\}\|_D^2 + h(x) \\ &\quad + \frac{1}{2\sigma^2} \|p - Ax + u\|^2, \end{aligned} \quad (13)$$

where σ is a tunable parameter, and u is the scaled dual variable. The ADMM algorithm for this problem can then be formulated as Algorithm 1.

Algorithm 1: ADMM formulation for coded exposure reconstruction

```

1 Initialize:  $p, x, u$ 
2 while not converged do
3    $p \leftarrow \arg \min_p L(p, x, u)$ 
4    $x \leftarrow \arg \min_x L(p, x, u)$ 
5    $u \leftarrow u + p - Ax$ 
6  $x^* \leftarrow x$ 

```

D. Modular Implementation

Note that the optimization sub-problems in Algorithm 1 can be simplified as

$$\begin{aligned} \arg \min_p L(p, x, u) &= \arg \min_p \left\{ \frac{1}{2} \|y + \log \{C \exp \{-p\}\}\|_D^2 \right. \\ &\quad \left. + \frac{1}{2\sigma^2} \|p - (Ax - u)\|^2 \right\}, \end{aligned} \quad (14)$$

$$\begin{aligned} \arg \min_x L(p, x, u) &= \arg \min_x \left\{ \frac{1}{2\sigma^2} \|(p + u) - Ax\|^2 \right. \\ &\quad \left. + h(x) \right\}. \end{aligned} \quad (15)$$

We can rewrite the optimization problems in equations (14) and (15) in a more compact form as

$$\arg \min_p L(p, x, u) = F_d(Ax - u), \quad (16)$$

$$\arg \min_x L(p, x, u) = F_t(p + u), \quad (17)$$

where the operators F_d and F_t are defined as

$$\begin{aligned} F_d(\tilde{p}) &= \arg \min_p \left\{ \frac{1}{2} \|y + \log \{C \exp \{-p\}\}\|_D^2 \right. \\ &\quad \left. + \frac{1}{2\sigma^2} \|p - \tilde{p}\|^2 \right\}, \end{aligned} \quad (18)$$

$$F_t(\tilde{p}) = \arg \min_x \left\{ \frac{1}{2\sigma^2} \|\tilde{p} - Ax\|^2 + h(x) \right\}, \quad (19)$$

where \tilde{p} is a representative variable.

Both operators F_d and F_t have intuitive interpretations. From its form, function F_d can be interpreted as the MAP deblurring function. Intuitively, F_d computes the MAP estimate of the micro-projections p given the coded blurred measurements y and a prior distribution of $N(\tilde{p}, \sigma^2 I)$. In other words, F_d is a function that recovers the full set of unobserved micro-projections in the proximity of \tilde{p} . On the other hand, the function $x = F_t(p)$ has the simple interpretation of being a function that computes the regularized tomographic reconstruction, x , given the micro-projections p .

Algorithm 2: CodEx reconstruction algorithm

```

1 Initialize:  $p, x, u$ 
2 while not converged do
3    $p \leftarrow \tilde{F}_d(Ax - u; p)$ 
4    $x \leftarrow \tilde{F}_t(p + u; x)$ 
5    $u \leftarrow u + p - Ax$ 
6  $x^* \leftarrow x$ 

```

Algorithm (2) shows the complete CodEx reconstruction algorithm. Since it is impractical to minimize the functions in equations (18) and (19) completely, we perform partial updates starting from an initial condition. The operator $\tilde{F}_d(\tilde{p}; p_{\text{init}})$ denotes the computation of $F_d(\tilde{p})$ for a fixed number of partial iterations starting from an initial condition of p_{init} . Similarly, the operator $\tilde{F}_t(\tilde{p}; x_{\text{init}})$ denotes the computation of $F_t(\tilde{p})$ for

a fixed number of partial iterations starting from an initial condition of x_{init} .

Algorithm 3 outlines the computation of the deblurring function, $\tilde{F}_d(\tilde{p}; p_{\text{init}})$ that performs a partial update minimization of equation (18) starting from an initial value of p_{init} . We use a gradient descent approach with a backtracking line-search [19] to perform the optimization. The cost function is denoted by

$$f_d(p) = \frac{1}{2} \|y + \log \{C \exp \{-p\}\}\|_D^2 + \frac{1}{2\sigma^2} \|p - \tilde{p}\|^2.$$

The gradient of the cost function $f_d(p)$ is denoted by

$$g = -\text{diag}(\exp \{-p\}) C^\top \text{diag}(C \exp \{-p\})^{-1} D e. \quad (20)$$

The cost function $f_d(\cdot)$ is evaluated several times for each iteration in order to choose an appropriate step-size of η starting from an initial step-size of η_0 .

Algorithm 3: Computation of the deblurring function

\tilde{F}_d

Input: Initial micro-projections: p_{init}

Proximal micro-projections input: \tilde{p}

Output: Final micro-projections: p^*

```

1 Initialize:  $p \leftarrow p_{\text{init}}$ 
2 for  $i \leftarrow 1$  to  $n_p$  do
3    $e \leftarrow y + \log \{C \exp \{-p\}\}$ 
4    $g = -\text{diag}(\exp \{-p\}) C^\top \text{diag}(C \exp \{-p\})^{-1} D e$ 
5    $\eta = \eta_0$ 
6   while  $f_d(p - \eta g) > f_d(p) - \eta \epsilon \|g\|^2$  do
7      $\eta \leftarrow \eta/2$ 
8    $p \leftarrow p - \eta g$ 
9  $p^* \leftarrow p$ 

```

Algorithm 4 outlines the computation of the tomographic reconstruction function, $\tilde{F}_t(\tilde{p}; x_{\text{init}})$ that performs a partial update minimization of equation (19) starting from an initial value of x_{init} . The optimization can be performed using any off-the-shelf software module that can perform regularized inversion. More implementation details are given in section V.

Algorithm 4: Computation of the tomographic reconstruction function \tilde{F}_t

Input: Initial reconstruction: x_{init}

Projections data: \tilde{p}

Output: Final reconstruction: x^*

```

1 Initialize:  $x \leftarrow x_{\text{init}}$ 
2 for  $i \leftarrow 1$  to  $n_t$  do
3    $e \leftarrow p - Ax$ 
4    $x \leftarrow x + \text{Update}(e, A)$ 
5  $x^* \leftarrow x$ 

```

Even though the coded deblurring and CT reconstruction problems are tightly coupled, the modular structure of Algorithm (2) separates them into deblurring and CT reconstruction sub-problems that must be solved repeatedly until convergence. Note that the deblurring operator F_d performs the

optimization in equation (18) purely in the projection domain and is independent of the CT geometry. Only the tomographic reconstruction operator F_t , and the forward projection operator A in Algorithm (2) depend on the CT geometry under consideration. Our approach can therefore be easily extended to other CT geometries by incorporating a different reconstruction operator F_t , and a forward projection operator A specific to that CT geometry.

IV. INTERLACED VIEW SAMPLING

Recently proposed interlaced view sampling schemes [2], [20] have demonstrated improved reconstruction quality for time-resolved tomography compared to traditional progressive view sampling. In interlaced view sampling, the view measurements are collected over multiple rotations of the object, rather than a single rotation as progressive sampling. This allows a wider range of angular measurements per unit time, thereby improving the reconstruction quality for time-resolved tomography [2].

Interlaced view sampling schemes typically require a large spacing between consecutive view angles, causing considerable motion blur in fly-scanning. CodEx is thus well suited for interlaced view sampling as the resulting motion blur can be inverted to improve the reconstruction quality.

However, using an irregularly spaced interlaced view sampling can make the CodEx reconstruction very computationally expensive. To see why this is, consider equation (3) that formulates the expected photon counts at a view-angle as a discrete sum over K micro-projection angles. If the view-angles are not regularly spaced, then the micro-projection angles for different view-angles will not match. In the worst case, the measurements at M_θ view-angles will be a function of $K M_\theta$ micro-projection angles. This increases the memory footprint of the projection domain variables $p, u \in \mathbb{R}^{K M_\theta M_d}$ in Algorithm 2 drastically, as well as increases the computational complexity of the operators F_d and F_t in equations (18) (19) considerably.

In order to improve the computational efficiency of CodEx reconstruction with interlaced views, we propose a interlaced view sampling scheme with regularly spaced view angles. The M_θ interlaced measurement angles are given as

$$\theta_i = \frac{\pi i K}{N_\theta}, \text{ for } i = 0, \dots, M_\theta - 1, \quad (21)$$

where K is the code length of coded exposure and N_θ is the number of unique micro-projection angles in $[0, \pi]$ chosen such that $\text{gcd}(K, N_\theta) = 1$. Not every choice of N_θ will yield a good interlaced angle scheme that offers a uniform coverage in the $[0, \pi]$ angular range. Theorem 1 in Appendix A shows that ensuring $\text{gcd}(K, N_\theta) = 1$ allows the view angles θ_i for $i = 0, \dots, N_\theta - 1$ to cover every unique angle $\frac{\pi j}{N_\theta}$ in $[0, \pi]$ for $j = 0, \dots, (N_\theta - 1)$. We refer to the view angling scheme in equation (21) for the case $M_\theta = N_\theta$ as dense view sampling since all the N_θ densely-spaced micro-projection angles are sampled in this case.

In order to ensure $\text{gcd}(K, N_\theta) = 1$, we choose N_θ in the following way

$$N_\theta = mK - n, \quad (22)$$

where the positive integers m and n are chosen so that n and K are co-primes. Once a suitable n is chosen that is co-prime to K , m can be adjusted to tune the angular spacing between view-angles. For a small n , the view-angles θ_i in equation (21) are roughly separated by $\frac{\pi}{m}$. Theorem 2 in Appendix A shows that our choice of N_θ satisfies the constraint $\gcd(K, N_\theta) = 1$. Some typical choices of the parameters K , m , n is given in Table I.

Code-length K	m	n	$N_\theta = mK - n$	Blur-angle $\Delta\theta = \frac{K180^\circ}{N_\theta}$
52	2	27	77	121.56°
52	5	27	233	40.17°
52	10	27	493	18.98°
52	20	27	1013	9.24°

Table I
TYPICAL PARAMETER CHOICES FOR VIEW-ANGLES

Fig 3 graphically illustrates the interlaced view-angle scheme in equation (21) for the case when $m = 5$, $n = 5$, and $K = 11$. In this case, there are $N_\theta = mK - n = 50$ distinct micro-projection angles in the range of $[0, \pi]$. Notice that each new measurement angle shown by a blue dot is spaced by $K = 11$ discrete angular steps, but the measurement angles do not repeat until all $N_\theta = 50$ distinct micro-projection angles are sampled.

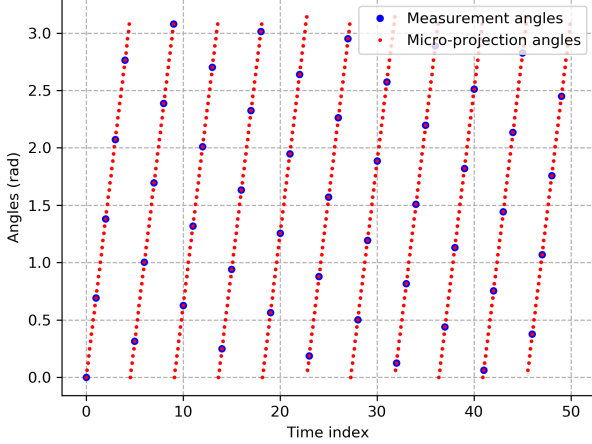


Figure 3. Illustration of our View angle sampling for coded exposure CT for $N_\theta = mK - n = 50$ ($K = 11$, $m = 5$, $n = 5$) and $M_\theta = 50$. Each new measurement angle shown by a blue dot is spaced by $K = 11$ discrete angular steps, but the measurement angles do not repeat until all $N_\theta = 50$ distinct micro-projection angles (blue dots) are sampled.

The expression of expected photon-counts at the detector given in equation (4) can be written more explicitly for the proposed interlaced view angle sampling as

$$\bar{\lambda}_i = \lambda^0 \sum_{k=0}^{K-1} c_k \exp \left\{ - \left(A_{\frac{\pi(iK+k)}{N_\theta}} \right) x \right\}, \text{ for } i = 0, \dots, M_\theta - 1, \quad (23)$$

where $\bar{\lambda}_i \in \mathbb{R}^{M_d}$ is the vector of expected photon-counts at the M_d detector pixels, λ^0 is the photon-flux of the X-ray source,

$c = [c_0, c_1, \dots, c_{K-1}]$ is the binary code used to modulate the photons, and $A_{\frac{\pi i K}{N_\theta}} \in \mathbb{R}^{M_d \times N}$ performs the forward projection of the image x at angle $\frac{\pi i K}{N_\theta}$.

In order to write equation (23) in a vectorized form, let us define $\bar{\lambda} \in \mathbb{R}^{M_d M_\theta}$ to be the vector of expected photon-counts at the detector for the M_θ measurement angles as

$$\bar{\lambda} = [\bar{\lambda}_0, \dots, \bar{\lambda}_{M_\theta-1}]^\top. \quad (24)$$

Let us also define the forward projection matrix for the N_θ micro-projection angles as

$$A = [A_0^\top, A_{\frac{\pi}{N_\theta}}^\top, \dots, A_{\frac{(N_\theta-1)\pi}{N_\theta}}^\top]^\top. \quad (25)$$

Using the above notation, equation (23) can be expressed in a more compact vectorized form like equation (4) as

$$\bar{\lambda} = \bar{c} \lambda^0 C \exp \{-Ax\}, \quad (26)$$

where $\bar{c} = \sum_{i=0}^{K-1} c_k$ is used for normalization, λ^0 is the photon-flux of the X-ray source, and the matrix C that performs the coded sum is defined as

$$C_{i(i_\theta, i_r, i_c), j(j_\theta, j_r, j_c)} = \begin{cases} \frac{c_k}{\bar{c}} & \text{if } \text{mod}(i_\theta K + k, N_\theta) = j_\theta \text{ for some } k < K, \\ & \text{and } i_r = j_r, \text{ and } i_c = j_c \\ 0 & \text{otherwise} \end{cases}, \quad (27)$$

where $\text{mod}()$ denotes the modulo operation and $i(i_\theta, i_r, i_c)$ represents the rasterized index i as a function of the angular index i_θ , row index i_r , and column index i_c . Similarly, $j(j_\theta, j_r, j_c)$ represents the rasterized index j as a function of the angular index j_θ , row index j_r , and column index j_c .

V. RESULTS

We present results using simulated and binned physical data in order to demonstrate the effectiveness for our CodEx approach. We consider three experimental cases outlined as follows:

- 1) Simulated data without noise
- 2) Simulated data with photon noise
- 3) Binned physical data.

In each experimental case, we compare the result of our Algorithm 2 to the baseline solution in equation (28) for different exposure codes. In particular, we consider three exposure codes:

- 1) Snapshot code: a single one followed by all zeros $(1, 0, \dots, 0)$
- 2) Raskar code [13]
- 3) Boxcar code: all ones $(1, 1, \dots, 1)$

Figure 4 displays these codes as a plot. The original Raskar code [13] is of length 52 but we extend it to larger code-lengths by repeating it by an integer number of times.

As a baseline method for comparison, we use an iterative reconstruction method without modelling the coded blur. Mathematically this can be written as

$$x_{\text{baseline}}^* = \arg \min_x \left\{ \frac{\lambda^0}{2} \sum_{i=0}^{M_\theta-1} \left\| y_i - A_{\frac{\pi i K}{N_\theta}} x \right\|^2 + h(x) \right\}, \quad (28)$$

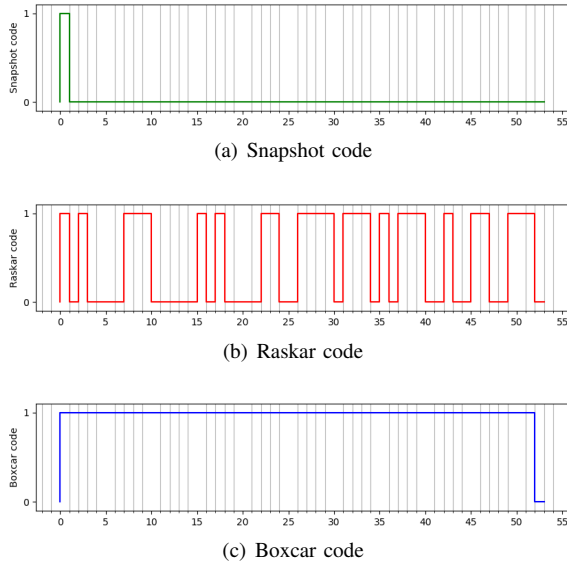


Figure 4. Examples of the binary codes of length 52 that are used for modulating the photon-flux in our experiments.

where $y_i \in \mathbb{R}^{M_d}$ is the vector of projection measurements at angle $\frac{\pi i K}{N_\theta}$ in accordance with the view sampling in equation (21), $A_{\frac{\pi i K}{N_\theta}} \in \mathbb{R}^{M_d \times N}$ performs forward projection of the image $x \in \mathbb{R}^N$ at angle $\frac{\pi i K}{N_\theta}$. The prior model $h(\cdot)$ is chosen to be the same as the CodEx reconstruction.

CodEx can utilize any off-the-shelf regularized inversion solver for F_t in equation (19) to compute the solution in Algorithm 2. The baseline method in equation (28) can similarly be computed using any off-the-shelf regularized inversion solver. In all our experimental results, we use svmbir (<https://github.com/cabouman/svmbir>) to compute F_t as well as the baseline reconstruction. The svmbir implementation uses a Markov random field based regularization and the reconstruction is computed using a cache optimized iterative coordinate descent [21], [22].

For computing the CodEx reconstruction, we run 1000 ADMM iterations in Algorithm 2. For each ADMM iteration, we run $n_p = 5$ partial updates for computing the \tilde{F}_d step and $n_t = 5$ partial updates for computing the \tilde{F}_t step. For computing the baseline reconstruction, we perform 400 iterations.

A. Simulated Data Without Noise

In this section we perform simulated experiments without noise in order to demonstrate the ability to deblur the coded blur introduced during the measurement process. We start with a phantom image, use forward-projection to generate simulated noise-free measurements, and then perform reconstruction from the simulated measurements. In order to generate simulated noise-free measurements, we make use of equations (4) and (5) with an infinitely large λ^0 . We set the diagonal elements of the weight matrix D to be 10^3 in equation (18). Details of the experimental setup are given in Table II.

Figure 5 provides a qualitative comparison between our method CodEx and the baseline for different exposure codes.

Number of Views, M_θ	233
Number of Unique Micro-projection Angles, N_θ	233
Angular Span	180°
Code Length, K	52
Blur Angle	40.17°
Reconstruction Size (x, y)	64×64

Table II
EXPERIMENTAL SETUP FOR SIMULATED DATA WITHOUT NOISE

For the Raskar and boxcar codes, the baseline reconstruction produces a blurred image. In contrast, CodEx is able to reconstruct the image without suffering from severe blurring. The CodEx-boxcar reconstruction has noticeable radial blur due to the non-invertible nature of the boxcar blur kernel. In contrast, the CodEx-Raskar and CodEx-snapshot reconstructions do not suffer from severe radial blur artifacts.

B. Simulated Data With Photon-noise

In this section, we perform simulated experiments with Poisson noise in order to simulate real coded-exposure tomographic systems. We start with a phantom image, use forward-projection to generate simulated noisy measurements, and then perform reconstruction from the simulated measurements. In order to generate simulated measurements, we make use of equations (4) and (5). The experimental details are summarized in Table III.

	λ^0	10000
Number of Views, M_θ	100	
Number of Unique Micro-projection Angles, N_θ	233	
Angular Span	180°	
Code Length, K	52	
Blur Angle	40.17°	
Reconstruction Size (x, y)	64×64	

Table III
EXPERIMENTAL SETUP FOR SIMULATED DATA WITH NOISE

Figure 6 shows a qualitative comparison of CodEx with the baseline for different coded exposures. For Raskar and boxcar codes, the baseline reconstruction leads to a blurred image. In contrast, CodEx-Raskar and CodEx-boxcar reconstructions do not suffer from severe blurring artifacts. The reconstructions with snapshot code suffer from high noise due to the limited photon counts in the measurements. The reconstructions with boxcar code suffer from radial blur artifacts and loss of fine features due to the non-invertible nature of the blur kernel.

In Figure 7, we plot the primal residual, $\text{RMSE}(Ax^t, p^t)$ and dual residual, $\text{RMSE}(Ax^t, Ax^{t-1})$ [18] at each ADMM iteration to illustrate the convergence of our method. Here t refers to the ADMM iteration number. The Raskar code leads to an improved convergence than the boxcar code.

In Figure 8, we show the effect of the photon-flux (λ^0) and the code length on reconstruction quality for different codes. For each code type snapshot, Raskar, and boxcar, we vary the photon-flux (λ^0) and plot the rmse with respect to the phantom to measure image quality. We also show the resulting image for a visual inspection of image quality. We repeat this process

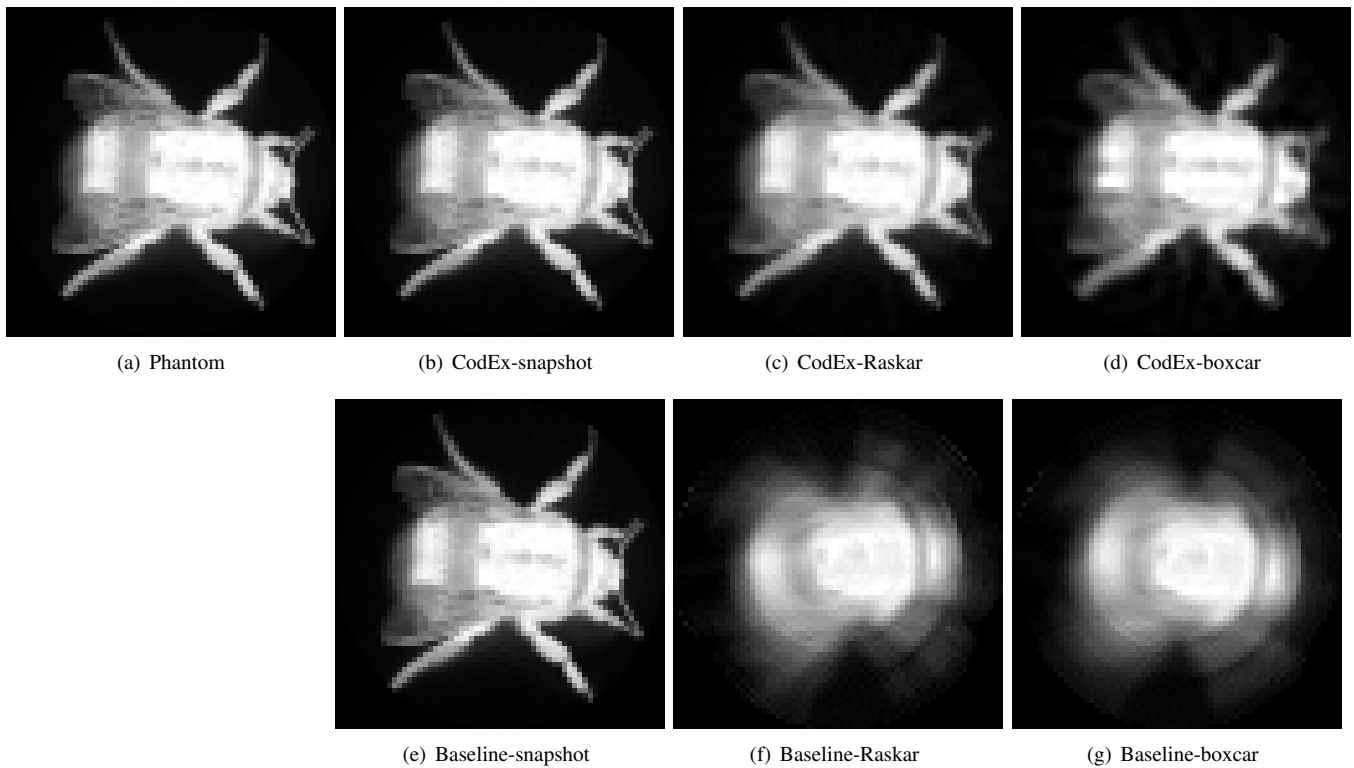


Figure 5. Comparison of reconstruction quality for simulated data without noise. Experimental details are in Table II. For the Raskar and boxcar codes, the baseline reconstruction produces a blurred image. In contrast, CodEx is able to reconstruct the image without suffering from severe blurring. The CodEx-boxcar reconstruction has noticeable radial blur due to the non-invertible nature of the boxcar blur kernel. In contrast, the CodEx-Raskar and CodEx-snapshot reconstructions do not suffer from severe radial blur artifacts.

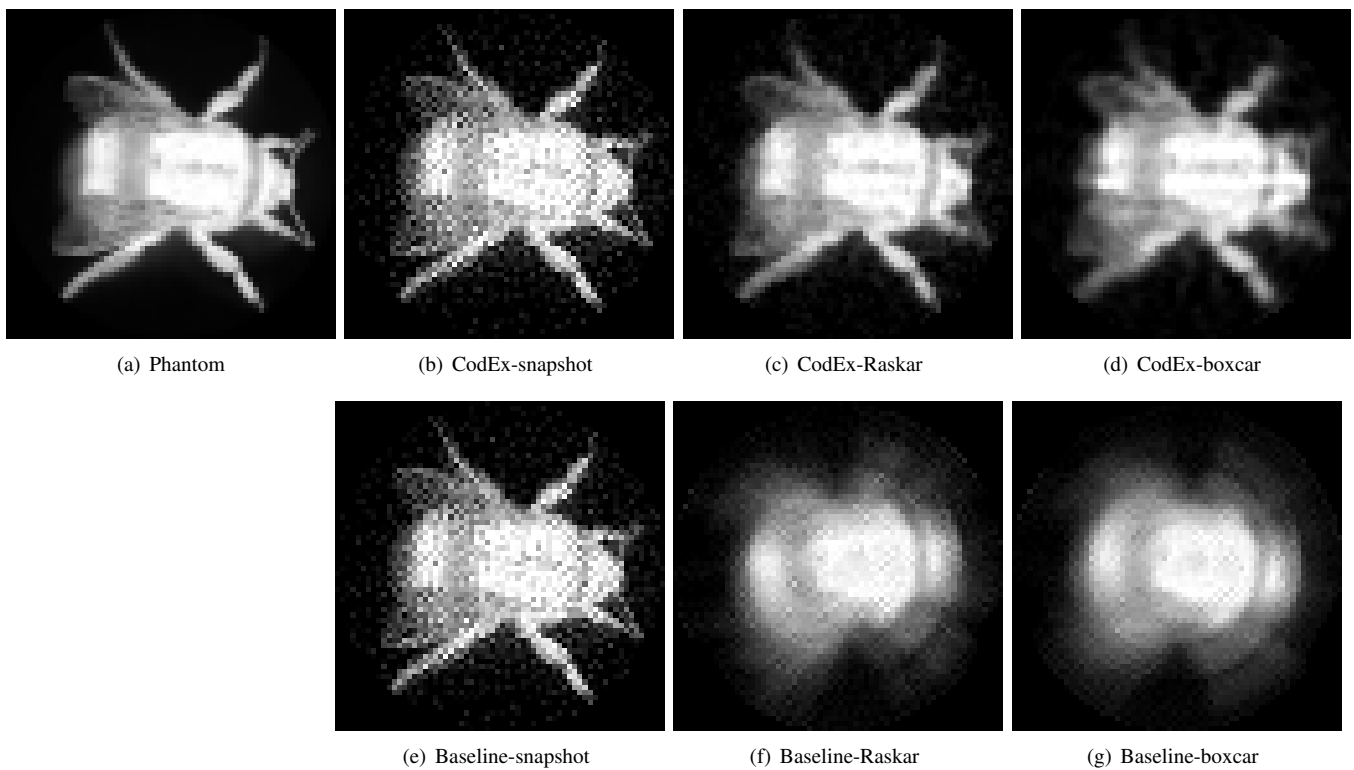


Figure 6. Comparison of reconstruction quality for simulated data with photon noise. Experimental details are in Table III. For Raskar and boxcar codes, the baseline reconstruction leads to a blurred image. In contrast, CodEx-Raskar and CodEx-boxcar reconstructions do not suffer from severe blurring artifacts. The reconstructions with snapshot code suffer from high noise due to the limited photon counts in the measurements. The reconstructions with boxcar code suffer from radial blur artifacts and loss of fine features due to the non-invertible nature of the blur kernel.

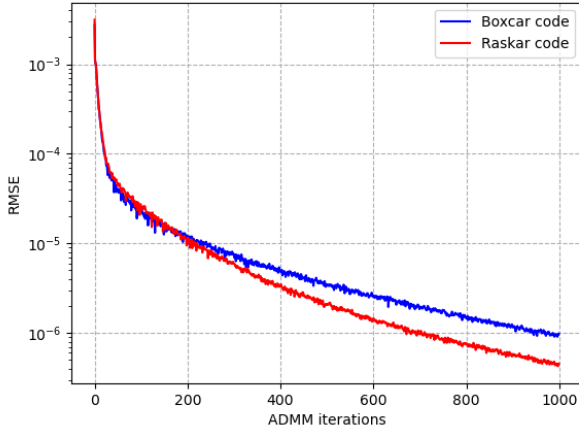
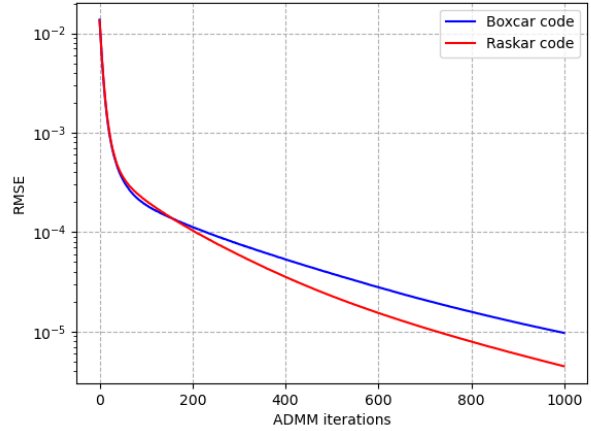
(a) Primal Residual: $\text{RMSE}(Ax^t, p^t)$ (b) Dual Residual: $\text{RMSE}(Ax^t, Ax^{t-1})$

Figure 7. Primal and dual residual convergence plots for simulated data with photon noise. Here t refers to the ADMM iteration number. The Raskar code leads to an improved convergence than the boxcar code.

for each code lengths of 52, 104, and 208. The remaining experimental parameters are kept the same as Table III. When the photon-flux (λ^0) is low, the boxcar code and Raskar code produce better image quality than the snapshot code as a result of collecting more photons. When the photon-flux (λ^0) is high, the minor gains from increased photon count do not fully compensate for the loss of information by inverting the coded blur. Consequently at high photon-flux, the snapshot code produce better image quality than the boxcar code and Raskar codes. Increasing the blur angle for a given photon-flux leads to the degradation of image quality for the boxcar code and Raskar codes since inverting the coded blur causes more loss of information. This loss of image quality is less pronounced for the Raskar code since the code is more invertible than the boxcar code. Consequently, when the photon-flux (λ^0) is low, increasing the blur angle for the Raskar code can be beneficial since the loss of information inverting the coded blur is compensated by the lower measurement noise due to increased photon collection.

	λ^0	40000
	Number of Views, M_θ	200
	Number of Unique Micro-projection Angles, N_θ	493
	Angular Span	180°
	Code Length, K	104
	Blur Angle	37.97°
	Reconstruction Size (x, y)	128×128

Table IV

EXPERIMENTAL SETUP FOR CHECKING ROBUSTNESS WITH RESPECT TO THE UNDERLYING OBJECT TO BE RECONSTRUCTED.

In order to show the robustness of our method, we perform simulated experiments using different widely-used natural images and CT images [23] as the phantom. For each phantom, we perform forward-projection to generate simulated noisy measurements and then perform reconstruction from the simulated measurements. To generate simulated measurements, we make use of equations (4) and (5). Experimental details are

summarized in Table IV. Figure 9 compares the CodEx reconstruction with the baseline reconstruction for each phantom image. The CodEx reconstruction is able to recover the major features of the image despite the high angular blur. In contrast, the baseline results in overtly blurred reconstructions.

C. Binned Experimental Data

In this section, we perform semi-simulated experiments by binning physical experimental data. Binning physical data allows us to generate arbitrary coded measurements without performing physical experiments using coded exposure. We start with an existing experimental data, generate coded measurements by binning, and then perform reconstruction from the coded measurements. The object in consideration contains borosilicate glass spheres of different sizes encased in a polypropylene matrix [24]. The experimental details are summarized in Table V.

	X-ray Energy	27.4 keV
	Exposure Time	0.0001 s
	Number of Views, M_θ	1500
	Number of Unique Micro-projection Angles, N_θ	1500
	Angular Span	180°
	Code Length, K	104
	Blur Angle	12.48°
	Pixel Size	$5.2 \mu\text{m}$
	Reconstruction Size (x, y)	320×320

Table V

EXPERIMENTAL SETUP FOR BINNED PHYSICAL DATA

Using the original experimental measurements at N_θ distinct view-angles, we generate $M_\theta = N_\theta$ coded measurements as

$$y_i = -\log \left\{ \sum_{k=0}^{K-1} \frac{c_k}{\bar{c}} \exp \left\{ -\tilde{y}_{\text{mod}(iK+k, N_\theta)} \right\} \right\}, \quad (29)$$

for $i = 0, \dots, N_\theta - 1$,

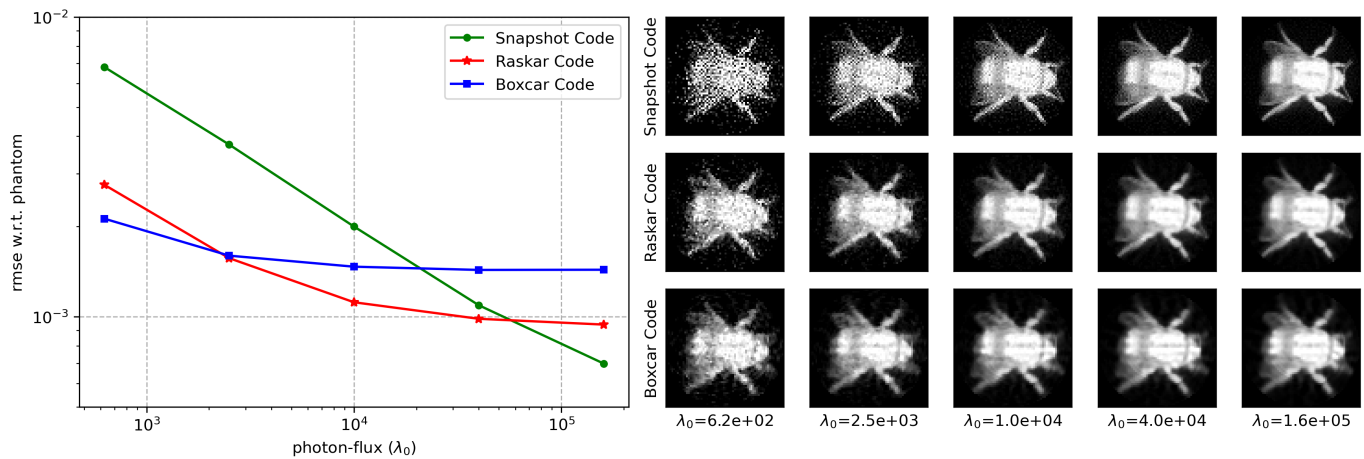
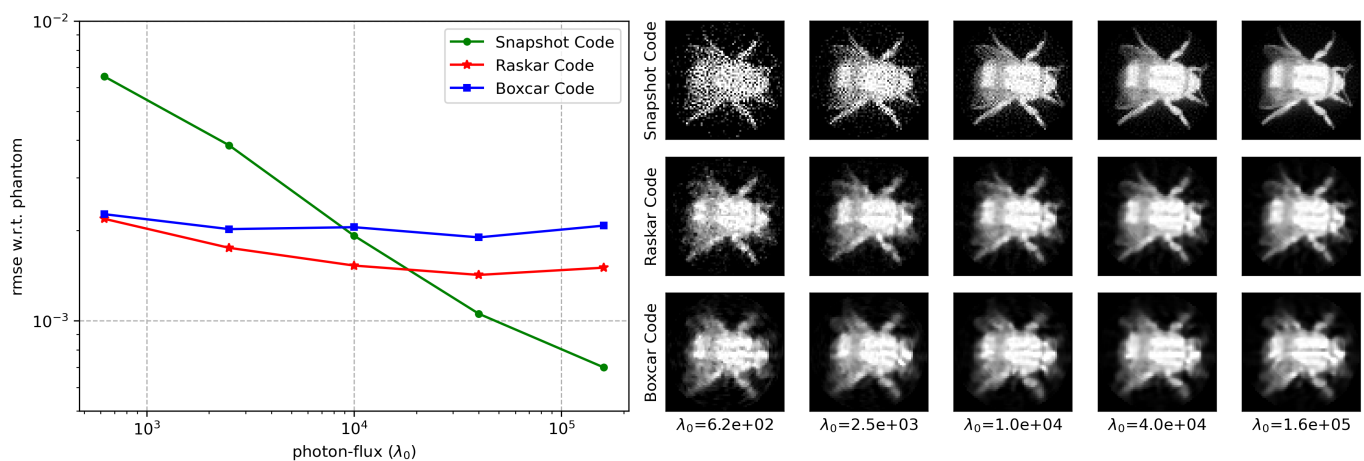
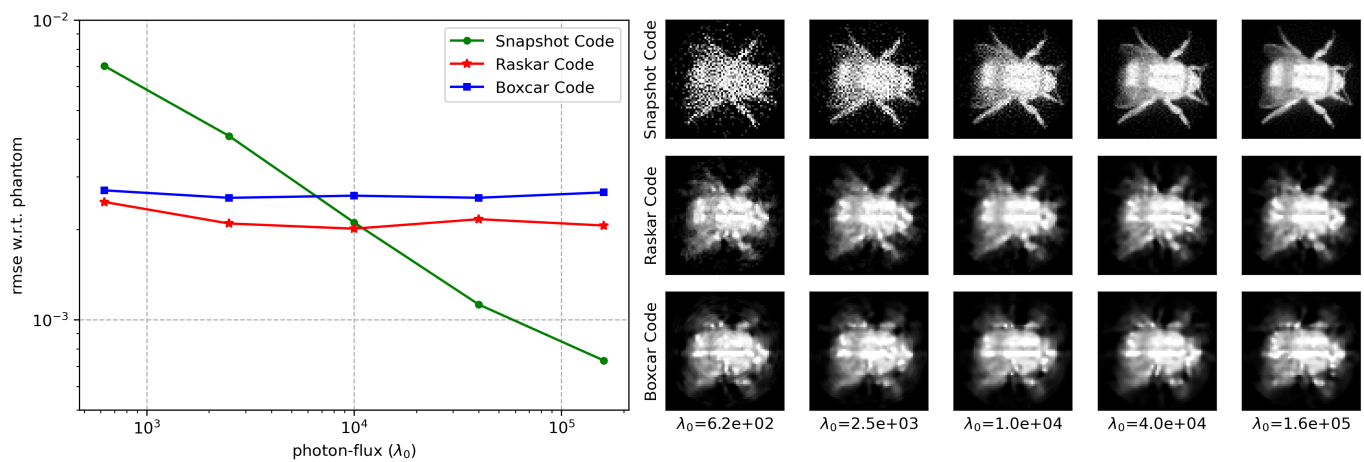
(a) Code length 52 (Blur angle 40.17°)(b) Code length 104 (Blur angle 80.34°)(c) Code length 208 (Blur angle 160.68°)

Figure 8. Effect of the photon-flux (λ^0) and the code length on reconstruction quality for different codes. The remaining experimental parameters are kept the same as Table III. When the photon-flux (λ^0) is low, the boxcar code and Raskar code produce better image quality than the snapshot code as a result of collecting more photons. When the photon-flux (λ^0) is high, the minor gains from increased photon count do not fully compensate for the loss of information by inverting the coded blur. Consequently at high photon-flux, the snapshot code produce better image quality than the boxcar code and Raskar codes.

where $\tilde{y}_{\text{mod}(iK+k, N_\theta)}$ is the vector of projection measurements at angle $\frac{\pi(iK+k)}{N_\theta}$ obtained from a physical experiment, y_i is the vector of coded measurements at the i^{th} view angle, $c = [c_0, \dots, c_{K-1}]$ is the binary code of length K . Note

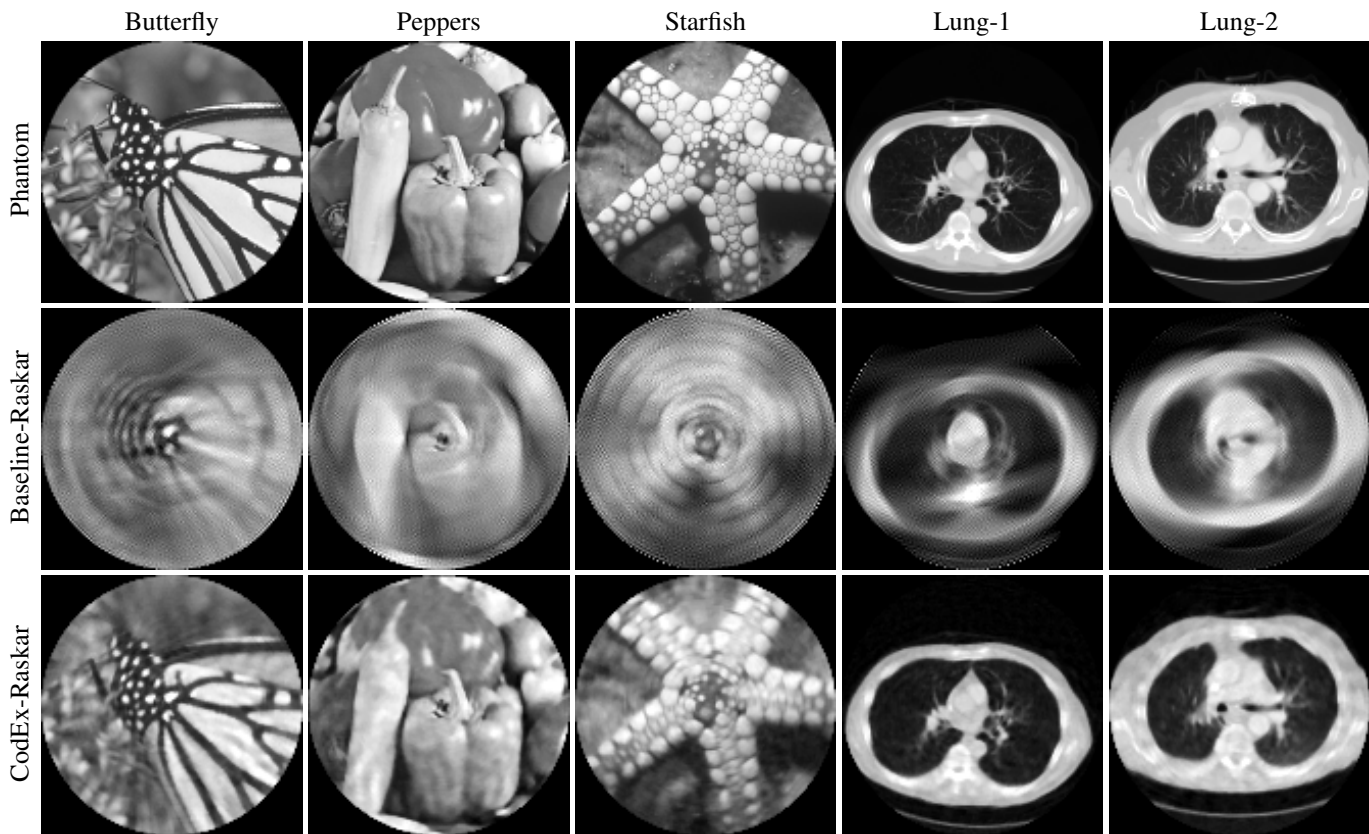


Figure 9. Robustness with respect to underlying reconstructed object. Experimental details are summarized in Table IV. The CodEx reconstruction is able to recover the major features of the image despite the high angular blur. In contrast, the baseline results in overtly blurred reconstructions.

that since we generate N_θ coded measurements from the N_θ original physical measurements, we can not create extra information by coding and our reconstruction quality with coded measurements can at best be that of using all the original measurements.

Figure 10 shows a comparison of our method with the baseline and the phantom for measurements with different exposure codes. For the Raskar and boxcar codes, direct reconstruction produces a blurred image. In contrast, our PnP coded exposure method is able to reconstruct the image without suffering from severe blurring.

In Figure 11 we plot the primal residual, $\text{RMSE}(Ax^t, p^t)$ and dual residual, $\text{RMSE}(Ax^t, Ax^{t-1})$ [18] at each ADMM iteration to illustrate the convergence of our method. Here t refers to the ADMM iteration number. The Raskar code leads to an improved convergence than the boxcar code.

VI. CONCLUSION

In this paper, we proposed CodEx, a novel method for coded exposure CT acquisition and reconstruction. CodEx can effectively invert the motion blur incurred during fly-scanning tomographic acquisition. Coding the exposure during acquisition can provide further improvements in the accuracy of the CodEx inversion. However, for certain applications the extra hardware for coding the exposure may not be necessary. For these applications, CodEx reconstruction can still lead to improvement in reconstruction quality by inverting the

non-coded motion blur. The modular structure of the CodEx reconstruction algorithm makes it practical to implement and easy to extend to different CT geometries.

APPENDIX

Theorem 1. All angles $\theta_i = iK \frac{\pi}{N_\theta}$ are unique (modulo π) if $0 \leq i \leq N_\theta - 1$ and $\text{gcd}(K, N_\theta) = 1$

Proof. Let us assume for the sake of contradiction that there are two integers i, j such that $i \neq j$, $0 \leq i, j \leq N_\theta - 1$, and $\theta_i = \theta_j$ (modulo π).

Using the definition of θ_i , this implies

$$iK = jK + c_1 N_\theta, \quad (30)$$

where c_1 is an integer constant. Rearranging equation (30), we have

$$(i - j)K = c_1 N_\theta. \quad (31)$$

Now since the left-hand-side of equation (31) is a multiple of K , so must be the right-hand-side. However, since $\text{gcd}(K, N_\theta) = 1$, c_1 must be a multiple of K . Let $c_1 = Kc_2$, for some integer constant c_2 . Then, equation (30) becomes

$$iK = jK + Kc_2 N_\theta. \quad (32)$$

Dividing by K on both sides give

$$i = j + c_2 N_\theta. \quad (33)$$

However, our initial assumption of $0 \leq i, j \leq N_\theta - 1$ is a direct contradiction to equation (33).

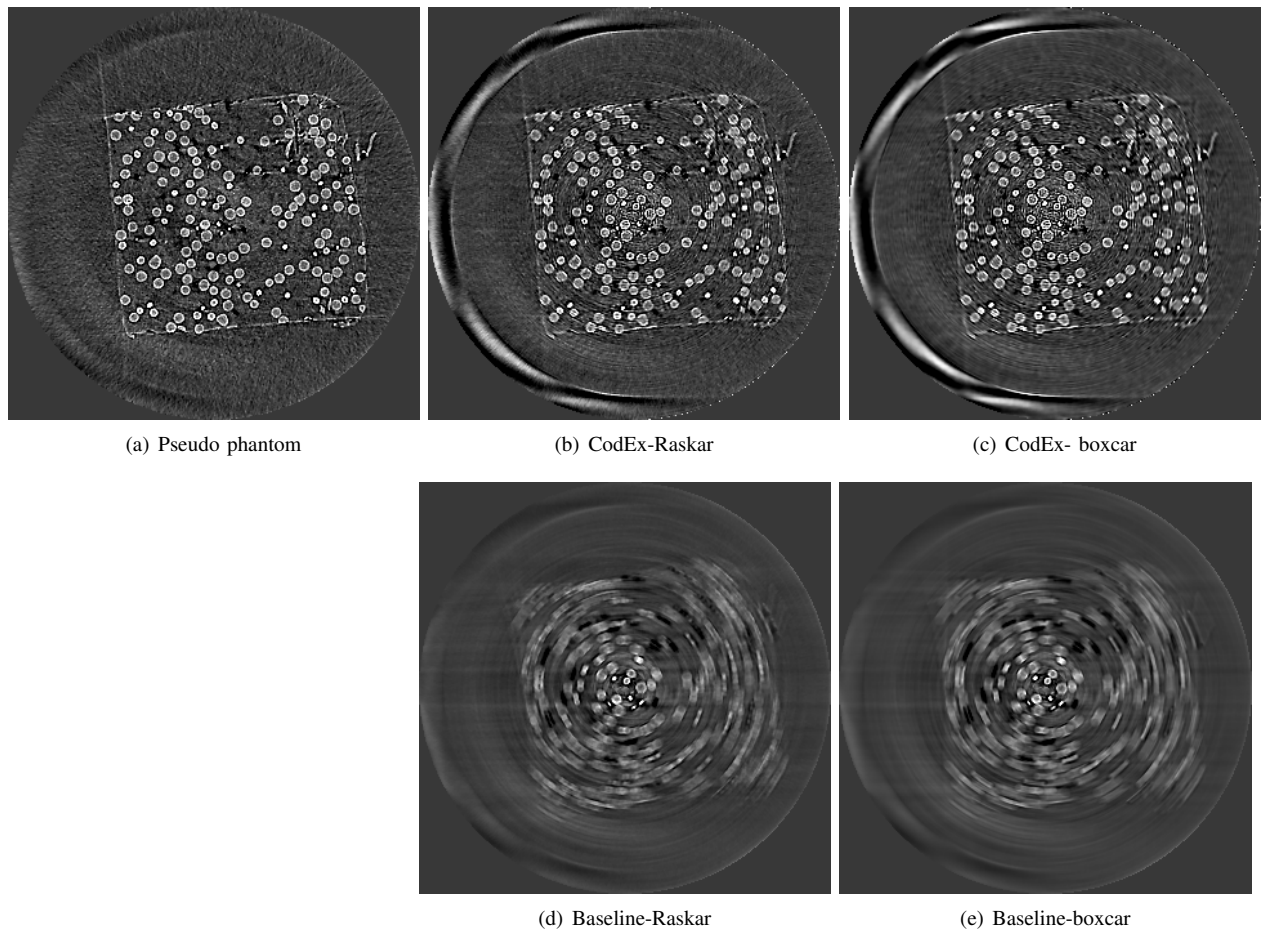


Figure 10. Comparison of reconstruction quality for binned physical data. Experimental details are summarized in Table V. CodEx reconstructions preserve the major features in the image whereas the baseline leads to overtly blurred reconstructions.

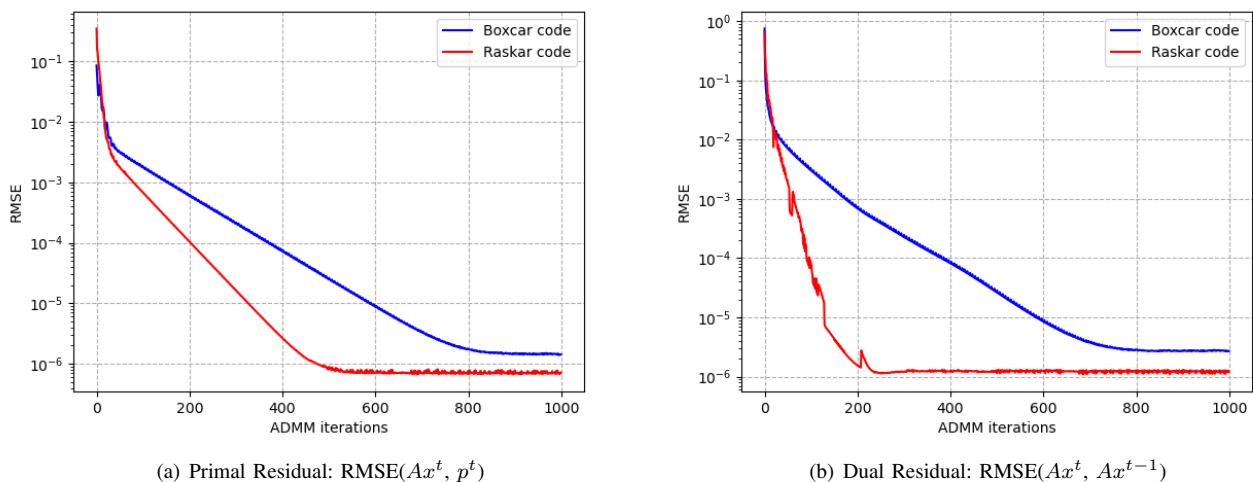


Figure 11. Primal and dual residual convergence plots for binned physical data. Here t refers to the ADMM iteration number. The Raskar code leads to an improved convergence than the boxcar code.

Theorem 2. If K, m, n are integers such that $\text{gcd}(K, n) = 1$ then $\text{gcd}(K, mK - n) = 1$

□ *Proof.* For the sake of contradiction let us assume $\text{gcd}(K, mK - n) \neq 1$ Thus we have $K = aq$ and $mK - n = bq$ for some integers a, b, q .

Therefore, $n = mK - bq = q(ma - b)$. Thus we have an

integer q that divides both K and n making $\gcd(K, n) \neq 1$ and leading to a contradiction. \square

REFERENCES

- [1] C. A. Bouman and K. Sauer, "A unified approach to statistical tomography using coordinate descent optimization," *IEEE Transactions on image processing*, vol. 5, no. 3, pp. 480–492, 1996.
- [2] K. A. Mohan, S. Venkatakrishnan, J. W. Gibbs, E. B. Gulsoy, X. Xiao, M. De Graef, P. W. Voorhees, and C. A. Bouman, "Timbir: A method for time-space reconstruction from interlaced views," *IEEE Transactions on Computational Imaging*, vol. 1, no. 2, pp. 96–111, 2015.
- [3] S. Majee, T. Balke, C. A. Kemp, G. T. Buzzard, and C. A. Bouman, "Multi-slice fusion for sparse-view and limited-angle 4D CT reconstruction," *IEEE Transactions on Computational Imaging*, vol. 7, pp. 448–461, 2021.
- [4] —, "4D X-Ray CT reconstruction using multi-slice fusion," in *2019 IEEE International Conference on Computational Photography (ICCP)*. IEEE, 2019, pp. 1–8.
- [5] D. J. Ching, M. Hidayetoğlu, T. Biçer, and D. Gürsoy, "Rotation-as-fast-axis scanning-probe x-ray tomography: the importance of angular diversity for fly-scan modes," *Applied optics*, vol. 57, no. 30, pp. 8780–8789, 2018.
- [6] M. Chang, Y. Xiao, Z. Chen, L. Li, and L. Zhang, "Preliminary study of rotary motion blurs in a novel industry CT imaging system," in *2011 IEEE Nuclear Science Symposium Conference Record*. IEEE, 2011, pp. 1358–1361.
- [7] D. Chen, H. Li, Q. Wang, P. Zhang, and Y. Zhu, "Computed tomography for high-speed rotation object," *Optics express*, vol. 23, no. 10, pp. 13 423–13 442, 2015.
- [8] J. Cant, W. J. Palenstijn, G. Behiels, and J. Sijbers, "Modeling blurring effects due to continuous gantry rotation: Application to region of interest tomography," *Medical Physics*, vol. 42, no. 5, pp. 2709–2717, 2015.
- [9] P. Gilbert, "Iterative methods for the three-dimensional reconstruction of an object from projections," *Journal of theoretical biology*, vol. 36, no. 1, pp. 105–117, 1972.
- [10] I. Steven Tilley, A. Sisniega, J. H. Siewerdsen, and J. W. Stayman, "High-fidelity modeling of detector lag and gantry motion in CT reconstruction," in *Conference proceedings. International Conference on Image Formation in X-Ray Computed Tomography*, vol. 2018. NIH Public Access, 2018, p. 318.
- [11] D. Ching, S. Aslan, V. Nikitin, and D. Gürsoy, "Time-coded aperture for x-ray imaging," *Optics Letters*, vol. 44, no. 11, pp. 2803–2806, 2019.
- [12] R. Gordon, R. Bender, and G. T. Herman, "Algebraic reconstruction techniques (art) for three-dimensional electron microscopy and x-ray photography," *Journal of theoretical Biology*, vol. 29, no. 3, pp. 471–481, 1970.
- [13] R. Raskar, A. Agrawal, and J. Tumblin, "Coded exposure photography: motion deblurring using fluttered shutter," in *ACM SIGGRAPH 2006 Papers*, 2006, pp. 795–804.
- [14] M. Pergament, M. Kellert, K. Kruse, J. Wang, G. Palmer, L. Wissmann, U. Wegner, and M. Lederer, "High power burst-mode optical parametric amplifier with arbitrary pulse selection," *Optics express*, vol. 22, no. 18, pp. 22 202–22 210, 2014.
- [15] M. Gembicky, D. Oss, R. Fuchs, and P. Coppens, "A fast mechanical shutter for submicrosecond time-resolved synchrotron experiments," *Journal of synchrotron radiation*, vol. 12, no. 5, pp. 665–669, 2005.
- [16] T. Balke, S. Majee, G. T. Buzzard, S. Poveromo, P. Howard, M. A. Groeber, J. McClure, and C. A. Bouman, "Separable models for cone-beam MBIR reconstruction," *Electronic Imaging*, vol. 2018, no. 15, pp. 181–1, 2018.
- [17] S. Majee, D. H. Ye, G. T. Buzzard, and C. A. Bouman, "A model based neuron detection approach using sparse location priors," *Electronic Imaging*, vol. 2017, no. 17, pp. 10–17, 2017.
- [18] S. Boyd, N. Parikh, E. Chu, B. Peleato, J. Eckstein *et al.*, "Distributed optimization and statistical learning via the alternating direction method of multipliers," *Foundations and Trends® in Machine learning*, vol. 3, no. 1, pp. 1–122, 2011.
- [19] L. Armijo, "Minimization of functions having lipschitz continuous first partial derivatives," *Pacific Journal of mathematics*, vol. 16, no. 1, pp. 1–3, 1966.
- [20] G. Zang, R. Idoughi, R. Tao, G. Lubineau, P. Wonka, and W. Heidrich, "Space-time tomography for continuously deforming objects," 2018.
- [21] X. Wang, K. A. Mohan, S. J. Kisner, C. Bouman, and S. Midkiff, "Fast voxel line update for time-space image reconstruction," in *2016 IEEE International Conference on Acoustics, Speech and Signal Processing (ICASSP)*. IEEE, 2016, pp. 1209–1213.
- [22] X. Wang, A. Sabne, P. Sakdhnagool, S. J. Kisner, C. A. Bouman, and S. P. Midkiff, "Massively parallel 3D image reconstruction," in *Proceedings of the International Conference for High Performance Computing, Networking, Storage and Analysis*, 2017, pp. 1–12.
- [23] B. Albertina, M. Watson, C. Holback, R. Jarosz, S. Kirk, Y. Lee, and J. Lemmerman, "Radiology data from the cancer genome atlas lung adenocarcinoma [TCGA-LUAD] collection," *The Cancer Imaging Archive*, 2016.
- [24] S. Singh, T. J. Stannard, S. S. Singh, A. S. Singaravelu, X. Xiao, and N. Chawla, "Varied volume fractions of borosilicate glass spheres with diameter gaussian distributed from 38-45 microns cased in a polypropylene matrix," Argonne National Lab.(ANL), Argonne, IL (United States), Tech. Rep., 2017.